ARTICLES SCIENCE CHINA Materials

mater.scichina.com link.springer.com

Published online 11 February 2018 | https://doi.org/10.1007/s40843-017-9226-5
Sci China Mater 2018, 61(8): 1078–1084

Unique redox properties in defective CeO_{2-x} nanocrystallines synthesized by laser melting

Lu Song[1], Jing Ma[1*], Qinghua Zhang[2], Yidan Cao[3], Rui Ran[3] and Zhijian Shen[1,4*]

ABSTRACT **Defects in cerium oxide, especially oxygen vacancies, play an essential role in its versatile applications and are efficiently preserved at ambient conditions in a non-equilibrium process. Herein, defective CeO_{2-x} with heterogeneous structure was synthesized by high-energy laser melting, where a large amount of oxygen vacancies and Ce^{3+} could be introduced, leading to improved visible light absorption, narrowed bandgap and room temperature ferromagnetism. Moreover, this laser melted CeO_{2-x} exhibits significantly enhanced low-temperature oxidation behaviors than the counterpart prepared by normal hydrogen-reduction. This unique redox performance could be attributed to the intragranular diffusion at the boundaries of assembled nanocrystallites. This method paves a new way for introducing unique multi-functions in oxide ceramics.**

Keywords: cerium oxide, laser melting, defect, boundary, redox property

INTRODUCTION

Materials prepared by non-equilibrium processes have often exhibited altered physical properties compared to their counterparts obtained at equilibrium conditions. This might be attributed to factors like altered microstructure, different phases or grains with defects. Nowadays, laser has been proven to be a powerful and versatile tool in non-equilibrium material processing. In case of high-energy laser modification of oxide ceramics this process would become even more complex, as the tendency of losing oxygen is remarkably enhanced under the high temperature by laser absorption at the material surface. Yet, this provides ideal conditions to introduce point defects in functional ceramics. Combining the abnormal behaviors of crystal growth, some unique characteristics, such as distribution of defects and their chemical activity under high temperature, could be preserved by the following rapid quenching. Thus, investigation on crystallographic features and functional performance of laser melted ceramics could promote our understanding of materials' behaviors under non-equilibrium state, while it may also act as a novel approach for synthesis of defective oxide ceramics.

An appropriate candidate for this study is CeO_2, which is known for the high structural tolerance of defects that play an essential role in its functional applications. The generation/elimination of oxygen vacancies, together with the corresponding alteration of valence state of Ce, leads to the widely-recognized oxygen storage capacity (OSC) that makes CeO_2 a highlight in catalysis research [1–4], and applications like photocatalysis and solid oxide fuel cells that significantly rely on the amount and mobility/diffusion of carriers, such as light absorption and band structure, while the generation of defects can be beneficial by inducing more carriers [5–9]. Thus, tailoring composition and morphology of pure and doped ceria has been a highlight in catalyst and electrolyte research [10–12]. Herein, induction of defects by laser melting and the corresponding effects on the redox performance of CeO_2 were studied in this research. A heterogeneous nanostructure, containing nanocrystallites with abundant oxygen vacancies, was found to be induced during laser melting that remarkably enhanced the low-temperature oxidation ability. The role of the interfacial diffusion through the high density of sub-grain boundary in nanocrystallines will be discussed in this article.

EXPERIMENTAL SECTION

Commercial CeO_2 nanopowder (Aladdin^{TM}), with a pur-

[1] State Key Lab of New Ceramics and Fine Processing, School of Materials Science and Engineering, Tsinghua University, Beijing 100084, China
[2] Beijing National Laboratory for Condensed Matter Physics, Institute of Physics, Chinese Academy of Sciences, Beijing 100190, China
[3] Key Lab of Advanced Materials (MOE), School of Materials Science and Engineering, Tsinghua University, Beijing 100084, China
[4] Department of Materials and Environmental Chemistry, Arrhenius Laboratory, Stockholm University, Stockholm 10691, Sweden
* Corresponding authors (emails: ma-jing@tsinghua.edu.cn (Ma J); shen@mmk.su.se (Shen Z))

ity of ≥99.95% and a mean particle diameter of 50 nm (information supplied by the manufacturer), was used as the precursor material. The ceria powder was compressed into pellets with no added organic binders to avoid explosion or residuals during laser melting. An ytterbium fiber laser (wavelength 1,071 nm) attached to a laser melting machine (AM 250, Renishaw, UK) was applied in the experiment, while the pellets were placed inside the closed chamber with pure Ar gas as the protective atmosphere (oxygen concentration below 2,000 ppm). The laser focused upon the pellets' top surface and the spot (75 μm in diameter and 50 W in laser power) moved along a scheduled path to fully melt the entire area. The energy density of the laser is about 600 J cm^{-2}, which is much higher than that normally used in laser ablation or annealing of ceramics [13,14]. The surface zone treated by laser was then carefully removed and ground into powder manually for characterization, and will be marked as "LT" in the following text.

X-ray photoelectron spectra (XPS) were recorded by a spectrometer (ESCALAB 250Xi, Thermo Fisher Scientific, USA) equipped with an Al Kα source (kinetic energy =1,486.7 eV). The C 1s peak (284.6 eV) was used for calibration. The crystallite structure was characterized by X-ray diffractometry (XRD, D/max 2500X, Rigaku Co, Japan) equipped with a Cu target. The transmission electron microscope (TEM) imaging and selected area electron diffraction (SAED) were performed using a TEM with a field emission gun (FEG-TEM, Tecnai G2 F20, FEI, USA), and an electron energy loss spectrometer (EELS) was also utilized to analyze the valence states. The accelerating voltage for TEM imaging and EELS was set to 200 kV.

Reflectance and bandgaps were measured by diffuse reflectance spectroscopy in the wavelength range of 250–750 nm conducted on a UV-vis spectrophotometer (U-3310, Hitachi, Japan). Magnetic properties were examined using a superconducting quantum interference device (SQUID-VSM, Quantum Design, USA) under the magnetic field between −10,000 and +10,000 Oe at 300 K. Specific surface area (S_{BET}) of the samples were measured by N_2 adsorption (SI-MP, Quadrasorb, USA) at 77.3 K. Before S_{BET} measurement, the samples were outgassed in vacuum at 100°C for 2 h to remove any adsorbed water or containments. Temperature programmed oxidation-temperature programmed reduction (TPO-TPR) experiments were performed by a chemisorption analyzer (AutoChem II 2920, Micromeritics, USA) to analyze the redox behaviors of ceria. About 50 mg sample was placed in a U-shaped quartz tube and pretreated in flowing He at 400°C for 30 min to remove absorbents, after which the sample was cooled down to 0°C. A mixture of 10% H_2/Ar (50 mL min^{-1}) was used in TPR, while 10% O_2/He (50 mL min^{-1}) was used in TPO. The temperature range for both experiments was 0–800°C with a heating rate of 10°C min^{-1}. Helium gas was used during all cooling processes.

RESULTS AND DISCUSSION

The XPS patterns of the pristine and laser melted CeO_2 samples were recorded (Fig. 1a, b). Due to the complexity of Ce 3d spectra, nonlinear least square fitting method of the obtained spectra was applied using standard spectra of Ce^{3+} and Ce^{4+} as references. It turns out that Ce^{3+} ions made no contribution to the spectra of the pristine sample, while 1/10 of the total cerium ions are Ce^{3+} after laser melting. Correspondingly, O 1s spectra for LT CeO_2 contain a weaker peak representing oxygen species related to defects (O(V), 530.3 eV) besides the major oxygen species presenting in lattice (O(L), ~529.0 eV) and chemisorbed hydroxyl groups (O(C), ~531.5 eV). The calculated peak areas correspond to around 12% content of O–Ce^{3+} and Ce^{3+} in LT CeO_2 sample. Additional information about the valence states was collected by EELS, as shown in Fig. 1c, d, respectively. For the Ce M-edge, the spectrum of the pristine sample is dominated by the Ce^{4+} feature, while an inversion in the intensity ratio of M_5/M_4 in the spectrum of LT CeO_2 is regarded as the symbol of higher Ce^{3+} content [15,16]. In the O K-edge spectrum of LT CeO_2, the intensity of the peak around 529.3 eV is much weaker, due to the additional electrons in 4f state where a Ce^{3+} ion broke the transition between O 1s state and a hybridized state of O 2p and Ce 4f levels [17]. As expected, the induced defects don't cause any obvious phase transformation, proven by the very similar CeO_2 diffractograms of the pristine and the laser treated samples (Fig. 1e). Sharp peaks of the cubic fluorite structure indicate good crystallinity. However, the peak positions for LT CeO_2 shift slightly towards lower 2θ angles compared to the pristine precursor (e.g. 59.060° in pristine CeO_2 and 58.920° in LT CeO_2 for (222) planes), indicating a slight lattice expansion of the cubic structure, which might be attributed to oxygen vacancies generated by rapid laser heating and cooling.

As XPS and EELS are sensitive to the chemical composition of surface materials, the overall abundance of defects implanted could be indicated by the changes of physical properties. For example, laser melting turns the light yellow pristine CeO_2 into opaque black (insets of Fig. 1e). The samples by laser-melting show much lower

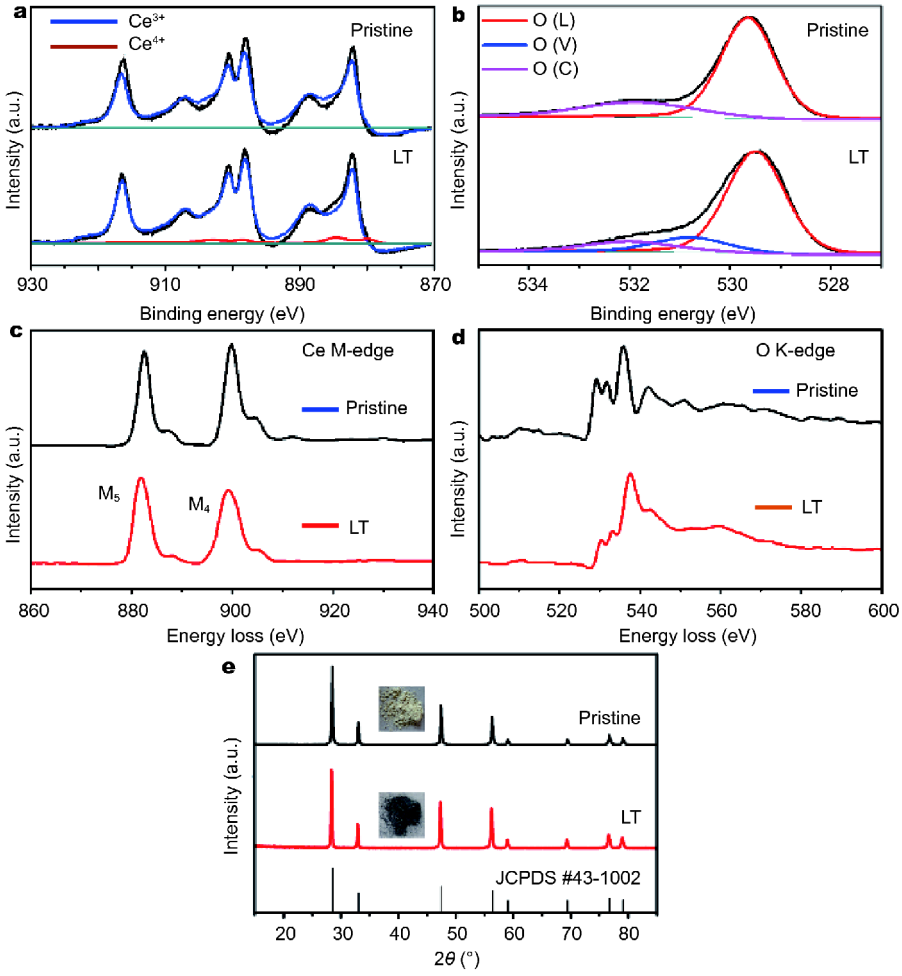

Figure 1 The XPS spectra of (a) Ce 3d and (b) O 1s of pristine and LT CeO_2 samples. The red curves above the baseline represent the existence of Ce^{3+} in the Ce 3d spectra. (c) Ce M-edge and (d) O K-edges in EELS for pristine and LT CeO_2. (e) XRD patterns of pristine and LT CeO_2 samples. Inset: photos of corresponding samples.

reflectance (about 20%) than pristine CeO_2 (exceed 80%) within UV-vis wavelength range (Fig. 2a). The deviation from stoichiometry has resulted in generation of color centers and higher absorption of electromagnetic radiation, which indicates the potential of better utilization of visible light in energy-conversion applications. Furthermore, by fitting Tauc plots, the value of bandgap could be collected, which was strongly narrowed from 3.17 eV in the pristine CeO_2 to 2.93 eV after laser melting (Fig. 2b). The accumulated defects also influence the magnetic properties, where a hysteresis loop clearly exhibits room temperature ferromagnetism in LT CeO_2, as shown in Fig. 2c. As no magnetic impurities were detected by XPS, this ferromagnetism seems to follow the F-center exchange (FCE) mechanism that oxygen vacancies with single positive charge (V_O^+/F^+ centers) were induced by the laser melting and ferromagnetism would arise once the density of F^+ centers reached the threshold to excite effective polaron interaction, which is favored by abundant defects in current case [18–20].

As the pristine CeO_2 was rapidly melted under inert atmosphere, generation of oxygen vacancies is sort of predictable like other reduction treatments, but what makes this laser melted CeO_2 unique is the heterogeneous grain morphology observed in TEM imaging (Fig. 3). While the size of pristine CeO_2 nanoparticles is more than 50 nm), the laser melted CeO_2 contains many crystallite sub-grains, as shown in Fig. 3a, b, respectively, demonstrating that intergrown crystallite areas have much smaller size than that of the precursor. Two sub-grain nanocrystallites with the continuous lattice fringe are presented in Fig. 3c. The identity of crystallographic or-

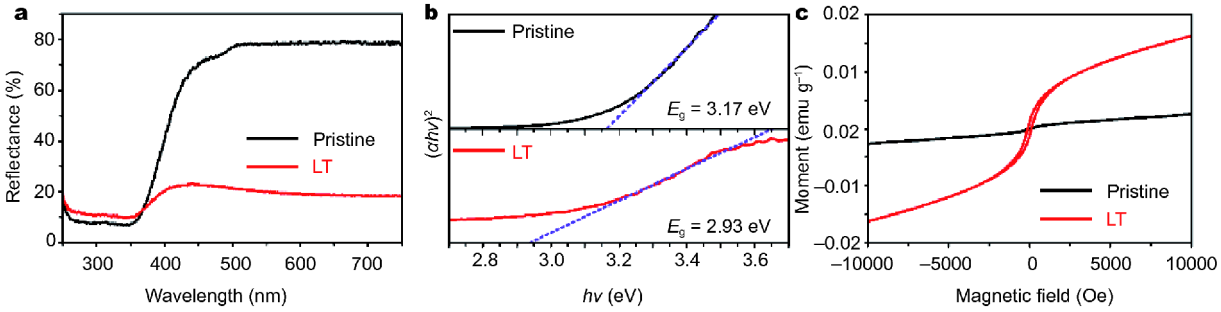

Figure 2 (a) UV-vis reflectance spectra and (b) Tauc plots and the fitted band gap of pristine and LT CeO_2 samples. (c) M–H curves of both samples.

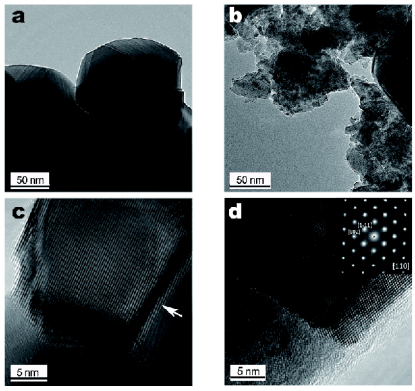

Figure 3 (a) TEM images of the pristine CeO_2. (b) Low-magnification TEM image of LT CeO_2. (c) and (d) HRTEM images of LT CeO_2. The white arrow points at the boundary between two nanocrystallites. Inset: SAED of the two adjacent nanocrystallites in (d).

ientation for adjacent nanocrystallites could be further verified by the independent diffraction spots in SAED shown in Fig. 3d, with no obvious transition phase detected along the boundary zone. These features in morphology are quite similar to those observed in mesocrystals formed by self-assembling, which might be the direct consequence of this nonequilibrium laser melting and cooling process (Fig. 3d), without obvious transition phase at the boundary. These features are quite similar to those observed in mesocrystals formed by self-assembling, probably due to nonequilibrium laser melting and cooling process [21]. Nanoparticles on the surface of pellets were melted instantly once the interaction with laser spot was initiated, and considering the oxygen-deficient circumstance, vigorous emission of oxygen is expected. The following rapid cooling process leads to suppressed grain growth of crystal nuclei during solidification process and the thermal stress which ruptures larger grains into the assemblies of nanocrystallites in the following cooling [21].

The abundant defects and assembled nanocrystallites facilitate us to investigate their redox performance by TPO-TPR experiments (Fig. 4). Two peaks of gas consumption exhibited in TPR curve of pristine CeO_2 (Fig. 4a): one peak at lower temperature (400–600°C) related to the reduction of surface oxygen species and the other at higher temperature (≥700°C) corresponding to the reduction of bulk oxygen [22,23]. In this case, while the H_2 consumption at high temperature is similar for these two samples, we noticed an obvious decrease in the low-temperature reduction in TPR curve of LT CeO_2. The decreased H_2 consumption at low-temperature can be attributed to the decreased outer surface area of the LT

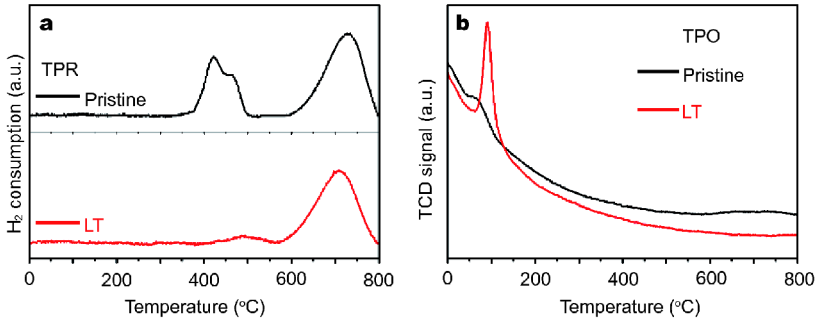

Figure 4 (a) Comparison in hydrogen consumption of the pristine and LT CeO_2 during TPR, (b) comparison in the original TCD signal in TPO measurement for pristine and LT CeO_2 (the same range of TCD signal is used).

CeO_2 powder as it was grounded manually, which is consistent with the S_{BET} measurement (2.0 m^2 g^{-1} for LT CeO_2 *vs.* 20.5 m^2 g^{-1} for pristine CeO_2). On the other hand, in TPO measurement, the reduced pristine CeO_2 showed a relatively smooth thermal conductivity detector (TCD) signal curve, indicating a relatively stable oxidation rate among the whole temperature range, while a significant oxidation peak around 100°C exhibited in the curve for LT CeO_2 (Fig. 4b). As the oxidation reaction in bulk is less efficient than the surface reaction, there should be some novel and highly-efficient approaches exist account for this fast low-temperature oxidation phenomenon in laser melted CeO_2.

In this way, we propose that intergranular diffusion through the boundaries of assembled LT CeO_2 nanocrystallites could be the origin of this unique redox behavior. Interfaces and boundaries are known to be nonstoichiometric intrinsically, due to the mismatch in crystallographic orientations and surface tension. Thus, high density of intergranular boundaries could sufficiently reduce the diffusion length for significant oxidation. Furthermore, in fluorite structure oxides such as ZrO_2 and CeO_2, the accumulation of oxygen vacancies along grain boundaries with space charge layers of negative potential alongside has been proved by the increased electrical conductivity, TEM [17,24–26] and experiments of quenching from high temperature also support this notion by preserving the high temperature defect structure [27]. The clusters of vacancies are beneficial to oxygen migration [28–30], and the space charge layer nearby could provide enough electrons (or polarons, Ce'_{Ce}) for the further reaction. Intergranular boundaries could act as the thermodynamically preferable routes of interfacial diffusion and shorten the diffusion path, and may also provide numerous low-energy reaction sites for the oxidation process [31], leading to the distinct redox behaviors of laser melted CeO_2. Besides, this unique redox performance of the laser treated CeO_2 could be preserved during redox cycles, revealing the stability in structure and performance.

CONCLUSION

In summary, we demonstrate that high-energy laser melting could induce the defective ceria nanocrystallites containing abundant oxygen vacancies, which would induce deep evolution in the physical properties and the redox behaviors of the CeO_{2-x}. The combination of altered chemical composition and multi-scale structures not only enhances the understanding of nonequilibrium processes and defect chemistry, but also has the potential to initiate deeper evolution in physical and chemical performance of oxide ceramics.

Received 16 November 2017; accepted 1 February 2018; published online 11 February 2018

1 Tuller HL. Defect structure and electrical properties of nonstoichiometric CeO_2 single crystals. J Electrochem Soc, 1979, 126: 209–217
2 Trovarelli A. Catalytic properties of ceria and CeO_2-containing materials. Catal Rev, 1996, 38: 439–520
3 Mogensen M. Physical, chemical and electrochemical properties of pure and doped ceria. Solid State Ion, 2000, 129: 63–94
4 Sun C, Li H, Chen L. Nanostructured ceria-based materials: synthesis, properties, and applications. Energy Environ Sci, 2012, 5: 8475–8505
5 Kharton VV, Figueiredo FM, Navarro L, *et al.* Ceria-based materials for solid oxide fuel cells. J Mater Sci, 2001, 36: 1105–1117
6 Rodriguez JA, Ma S, Liu P, *et al.* Activity of CeO_x and TiO_x nanoparticles grown on Au(111) in the water-gas shift reaction. Science, 2007, 318: 1757–1760
7 Ratnasamy C, Wagner JP. Water gas shift catalysis. Catal Rev, 2009, 51: 325–440
8 Primo A, Marino T, Corma A, *et al.* Efficient visible-light photocatalytic water splitting by minute amounts of gold supported on nanoparticulate CeO_2 obtained by a biopolymer templating method. J Am Chem Soc, 2011, 133: 6930–6933
9 Wang Z, Jiang S, Li Y, *et al.* Highly active CeO_2 hollow-shell spheres with Al doping. Sci China Mater, 2017, 60: 646–653
10 Chen D, Ran R, Zhang K, *et al.* Intermediate-temperature electrochemical performance of a polycrystalline $PrBaCo_2O_{5+\delta}$ cathode on samarium-doped ceria electrolyte. J Power Sources, 2009, 188: 96–105
11 Huang C, Wu X, Ren W, *et al.* Preparation of CeO_2 micro/nanostructure and their photocatalytic properties in glow discharge electrolysis. Ceramics Int, 2015, 41: S47–S50
12 Zhang Y, Shi R, Yang P, *et al.* Fabrication of electronspun porous CeO_2 nanofibers with large surface area for pollutants removal. Ceramics Int, 2016, 42: 14028–14035
13 Luo GP, Chen CL, Chen SY, *et al.* Fabrication of micro and submicro Y–Ba–Cu–O particles by excimer laser processing. J Vac Sci Technol A, 2000, 18: 2598
14 Bayati R, Molaei R, Richmond A, *et al.* Modification of properties of yttria stabilized zirconia epitaxial thin films by excimer laser annealing. ACS Appl Mater Interfaces, 2014, 6: 22316–22325
15 Garvie LAJ, Buseck PR. Determination of Ce^{4+}/Ce^{3+} in electron-beam-damaged CeO_2 by electron energy-loss spectroscopy. J Phys Chem Solids, 1999, 60: 1943–1947
16 Gao P, Wang Z, Fu W, *et al. In situ* TEM studies of oxygen vacancy migration for electrically induced resistance change effect in cerium oxides. Micron, 2010, 41: 301–305
17 Winterstein JP, Carter CB. Electron-beam damage and point defects near grain boundaries in cerium oxide. J Eur Ceramic Soc, 2014, 34: 3007–3018
18 Coey JMD, Venkatesan M, Fitzgerald CB. Donor impurity band exchange in dilute ferromagnetic oxides. Nat Mater, 2005, 4: 173–179
19 Hong NH, Sakai J, Poirot N, *et al.* Room-temperature ferromagnetism observed in undoped semiconducting and insulating oxide thin films. Phys Rev B, 2006, 73: 132404

20 Chen SY, Tsai CH, Huang MZ, *et al.* Concentration dependence of oxygen vacancy on the magnetism of CeO_2 nanoparticles. J Phys Chem C, 2012, 116: 8707–8713
21 Qian B, Xiao C, Zou J, *et al.* Assembled nano-structures from micron-sized precursors. RSC Adv, 2014, 4: 30754–30757
22 Zhou K, Wang X, Sun X, *et al.* Enhanced catalytic activity of ceria nanorods from well-defined reactive crystal planes. J Catal, 2005, 229: 206–212
23 Chen D, Cao Y, Weng D, *et al.* Defect and transport model of ceria–zirconia solid solutions: $Ce_{0.8}Zr_{0.2}O_{2-\delta}$ — An electrical conductivity study. Chem Mater, 2014, 26: 5143–5150
24 Kim S, Maier J. On the conductivity mechanism of nanocrystalline ceria. J Electrochem Soc, 2002, 149: J73
25 Lei Y, Ito Y, Browning ND, *et al.* Segregation effects at grain boundaries in fluorite-structured ceramics. J Am Ceramic Soc, 2002, 85: 2359–2363
26 Guo X, Waser R. Electrical properties of the grain boundaries of oxygen ion conductors: Acceptor-doped zirconia and ceria. Prog Mater Sci, 2006, 51: 151–210
27 Barhmi AE, Schouler EJL, Hammou A, *et al.* Influence of quenching on the electrical properties of yttria-stabilized zirconia. Solid State Ion, 1988, 28-30: 493–496
28 Esch F, Fabris S, Zhou L, *et al.* Electron localization determines defect formation on ceria substrates. Science, 2005, 309: 752–755
29 Liu X, Zhou K, Wang L, *et al.* Oxygen vacancy clusters promoting reducibility and activity of ceria nanorods. J Am Chem Soc, 2009, 131: 3140–3141
30 Skorodumova NV, Simak SI, Lundqvist BI, *et al.* Quantum origin of the oxygen storage capability of ceria. Phys Rev Lett, 2002, 89: 166601
31 Chiang YM. Nonstoichiometry and electrical conductivity of nanocrystalline CeO_{2-x}. J Electroceramics, 1997, 1: 205–209

Acknowledgements We thank Dr. Jiang H (Center for Testing & Analyzing of Materials, School of Materials Science and Engineering, Tsinghua University) for the help in XPS data processing and analyzing, and Prof. Chen C and Prof. Thommy Ekstrom for valuable advices and revising the manuscript. This work was supported by the National Natural Science Foundation of China (51272124 and U1605243).

Author contributions Shen Z and Ma J conceived the idea of this project. Song L performed the synthesis of materials and XPS, XRD, and measurement of optical and electrical properties. Zhang Q performed the TEM experiments. Ran R and Cao Y designed and performed TPO-TPR experiments.

Conflict of interest The authors declare that they have no conflict of interest.

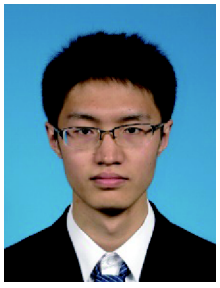

Lu Song is currently a PhD candidate in the School of Materials Science and Engineering, Tsinghua University. His current study focuses on the effects of laser melting on the microstructure and functional performance of oxide ceramics.

Zhijian Shen is a joint professor in Tsinghua University and Stockholm University. He has long been engaged in the research of material chemistry and manufacturing engineering, and has conducted systematic research work in the fields of advanced ceramic materials, biomaterials and nanomaterials. His current research focuses on increasing the complexity of material structures through additive manufacturing or biomimetic design to improve material properties and multi-functional composites.

Jing Ma is an assistant professor in the School of Materials Science and Engineering, Tsinghua University. Her researches include high performance multiferroic composites and device prototypes, oxide heterostructures and novel micro-structure and functional properties of oxide ceramics.

激光熔融合成CeO_{2-x}纳米晶的氧化还原性能

宋路[1], 马静[1*], 张庆华[2], 曹译丹[3], 冉锐[3], 沈志坚[1,4*]

摘要 本文采用高能激光熔化技术制备出具有非平衡非均匀结构的CeO_{2-x}纳米晶. 大量氧空位和Ce^{3+}的引入使可见光吸收率提升, 禁带宽度变窄及室温铁磁性增强. 此外, 与通常氢还原的样品比较, 这种激光熔融得到的CeO_{2-x}呈现出增强的低温氧化能力. 这种独特的氧化还原行为可归因于通过并聚的纳米晶的晶界扩散. 这一方法为多功能氧化物陶瓷的制备提供了一条新的途径.

